



Effect of temperature on small-scale deformation of individual face-centered-cubic and body-centered-cubic phases of an $\text{Al}_{0.7}\text{CoCrFeNi}$ high-entropy alloy

Adenike M. Giwa^a, Zachary H. Aitken^{b,*}, Peter K. Liaw^c, Yong-Wei Zhang^b, Julia R. Greer^{a,*}

^a Division of Engineering and Applied Sciences, California Institute of Technology, Pasadena, CA 91106, USA

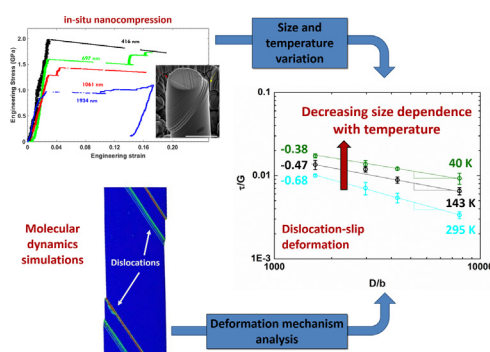
^b Institute of High Performance Computing (IHPC), A*STAR, 138632, Singapore

^c Department of Materials Science and Engineering, The University of Tennessee, Knoxville, TN 37996, USA

HIGHLIGHTS

- Both phases of a dual-phase $\text{Al}_{0.7}\text{CoCrFeNi}$ high entropy alloy display a “smaller is stronger” size effect at 295 K, 143 K, and 40 K.
- The size effect decreases in the face-centered cubic phase while remaining constant in the body-centered cubic phase as temperature decreases.
- The decreasing size-effect in the face-centered cubic phase is a result of increasing lattice friction stress with decreasing temperature.

GRAPHICAL ABSTRACT



ARTICLE INFO

Article history:

Received 17 December 2019

Received in revised form 18 February 2020

Accepted 27 February 2020

Available online 28 February 2020

Keywords:

High-entropy alloys
Cryogenic temperature
Deformation mechanisms
 $\text{Al}_{0.7}\text{CoCrFeNi}$
Nanopillars
Dislocations
Nanoplasticity

ABSTRACT

High-entropy alloys (HEAs) represent an important class of structural materials because of their high strength, ductility, and thermal stability. Understanding the mechanical response of isolated phases of a FCC/BCC dual-phase HEA is integral to understanding the mechanical properties of these alloys in the bulk. We investigate the compressive response of single-crystalline cylinders with diameters between 400 nm and 2 μm excised from individual grains within FCC and BCC phases of the dual-phase $\text{Al}_{0.7}\text{CoCrFeNi}$ HEA at 295 K, 143 K, and 40 K. We observed a “smaller is stronger” size effect in the yield strength as a function of pillar diameter, D , and 40 K. We investigated a power-law relationship, $\sigma_y \propto D^{-m}$, with a power-law exponent, m , decreasing with temperature for the FCC phase, and remaining constant for all temperatures in the BCC phase. We found reduced work-hardening rates and more extensive strain bursts during deformation at lower temperatures in all samples. We performed molecular dynamics simulations of similar FCC and BCC HEA compression that displayed deformation dominated by dislocation slip at all temperatures. We discussed theories of low-temperature strengthening in HEAs, compared them to our experimental data and assessed how they manifest in the observed temperature-dependent size effect and work-hardening.

© 2020 Published by Elsevier Ltd. This is an open access article under the CC BY-NC-ND license (<http://creativecommons.org/licenses/by-nc-nd/4.0/>).

* Corresponding authors.

E-mail addresses: zach-aitken@ihpc.a-star.edu.sg (Z.H. Aitken), jrgreer@caltech.edu (J.R. Greer).

1. Introduction

High-entropy alloys (HEAs) are a class of alloys that contain multiple elements in equi- or near equi-atomic proportions. These alloys were first developed by Yeh, et al. and Cantor, et al. in 2004 and found to display substantially higher strength, ductility, and wear resistance, compared to conventional alloys [1–5]. Improved mechanical properties of HEAs stem from the large lattice distortions and sluggish diffusion within their atomic microstructures [6]. Identifying and predicting stable HEA compositions and their associated properties have been challenging because the fundamental properties of individual elements and phases need to be understood in addition to the complex interactions of their combinations, which could sometimes lead to the formation of intermetallics and amorphous phases [7]. Some attempts have been made to classify HEAs based on their crystal structures and mechanical behaviour [8], and several studies on microstructural evolution with minor-element alloying provide some insights into understanding stable HEA microstructures [9–13]. HEAs often exhibit particularly interesting properties at extreme conditions. Eutectic and near-eutectic HEAs show good castability and display high strengths and ductility at elevated and cryogenic temperatures [14–16]. The mechanical properties of these HEAs have also shown to be compositional robust [15]. For example, the CrMnFeCoNi HEA undergoes a face-centered-cubic to hexagonal-close-packed (FCC-HCP) phase transformation induced by the extensive stacking fault formation at pressures >14 GPa [17]. The same CrMnFeCoNi HEA was reported to have a tensile strength of 1 GPa and a fracture toughness of $200 \text{ MPa}\cdot\sqrt{\text{m}}$, as well as tensile deformability over a 7% strain at 77 K, compared with 5% at room temperature, enabled by deformation twinning [18]. Excellent fracture toughness at room temperature has also been explained in this same HEA as a combination of several dislocation mechanisms that include the partial dislocation slip and dislocation-barrier formation, formation of stacking-fault parallelepipeds, and nano-scale twinned regions spanning the crack tip [19]. This feature demonstrates that HEAs make use of multiple plastic-deformation mechanisms to achieve their favourable mechanical properties.

To identify and quantify the contributions of different microstructural parameters, such as the dislocation density, grain size, stacking fault energy, propensity for twin formation, etc. to the mechanical response of bulk metals, conventional practice has been to conduct systematic experiments on small-scale samples [20]. Small-scale experiments are also useful for the design of nanoelectromechanical systems (NEMS) and microelectromechanical systems (MEMS) [21–23]. In addition to investigating deformation at room temperature, exploring the effect of temperature on the deformation of HEAs is also essential for aerospace applications, satellite parts, and tanks for liquefied gases.

In our earlier work, micro-sized pillars excised from individual FCC and body-centered-cubic (BCC) phases of the same $\text{Al}_{0.7}\text{CoCrFeNi}$ alloy were compressed at room temperature and revealed different mechanical behaviour between the two phases. The BCC nano- and micro-pillars exhibited continuous plastic flows and high axial strengths, for example $2.2 \pm 0.24 \text{ GPa}$ for 400-nm-sized [001]-oriented pillars; FCC samples had stochastic strain bursts throughout deformation and lower yield strengths, e.g., $1.2 \pm 0.13 \text{ GPa}$ for [324]-oriented pillars of equivalent size [24]. In the present work, we performed in-situ uniaxial compression experiments on micro- and nano-pillars with diameters ranging from 394 nm to 2114 nm made from FCC and BCC phases of this same alloy at temperatures of 40 K, 143 K, and 295 K to investigate the relative contributions of temperature and sample size under compressive loading. Our experiments demonstrate that the yield strength of 400-nm-sized [324]-oriented FCC pillars deformed at 40 K is $2.0 \pm 0.19 \text{ GPa}$ and that for [001]-oriented BCC pillars is $3.2 \pm 0.28 \text{ GPa}$. We observed power-law strengthening with decreasing sample size at each temperature, with a size-effect exponent of $m = 0.33$ at all temperatures for BCC samples; a decreasing m of 0.68 to 0.47 and to

0.38 as the temperature was reduced from 298 K to 143 K and to 40 K for the FCC samples, respectively. Transmission electron microscopy (TEM) analysis of the deformed pillars shows dislocations and their networks present in all the samples. To provide insight into the dominant deformation mechanisms present in experiments, we also performed molecular dynamics (MD) simulations of compression on similar FCC and BCC HEA nanopillars. In simulations, we observed that deformation is driven by the nucleation of partial dislocations from the surface of these initially-pristine nanopillars.

2. Materials and methods

The $\text{Al}_{0.7}\text{CoCrFeNi}$ HEA was fabricated using the vacuum arc-melting method with powders (Al, Co, Cr, Fe, and Ni) of 99% purity in weight percent. Details of this process are described in [24]. The crystallographic phase and orientation information were identified using the HKL Electron Back Scatter Diffraction system coupled to a ZEISS Scanning Electron Microscope. The bulk HEA displays a dendritic structure where dendrite regions have a Fe, Cr, and Co-rich FCC lattice, and interdendrite regions have an Al, Ni-rich BCC lattice [24]. The TEM analysis of the BCC phase further indicates the presence of a disordered A2 lattice and ordered B2 phases. This microstructure is consistent with previous reports for the $\text{Al}_x\text{CoCrFeNi}$ HEA system [9,13]. The nanopillars were fabricated from individual grains with a [324] orientation for the FCC phase and [001] orientation for the BCC phase using the FEI Versa three-dimensional (3D) dual scanning electron microscope (SEM) equipped with a focused ion beam (FIB). The fabrication details for making concentric circular milling pillars with the desired diameters of 394 nm to 2114 nm and a 3 (height): 1 (diameter) aspect ratio can be found in [24]. A typical pillar taper angle was estimated to be 2–3° and no >5° for all pillars of any size.

We conducted nanomechanical experiments in an in-situ instrument, which consists of a nanomechanical module (InSEM™, Nanomechanics Inc.) inside a SEM (FEI Quanta 200 FEG), with a cryogenic assembly (Janis research company), which has a vacuum transfer line that can be connected to either liquid helium or liquid nitrogen to control the temperature. This cryogenic assembly is equipped with a temperature controller containing thermocouples to read the temperature at the cold finger entry to the SEM chamber and at the sample stage. Room-temperature experiments were conducted in the same setup without the cryogenic assembly. A detailed description of the cryogenic-testing methodology can be found in Lee, et al. [23]. A constant temperature of ~143 K was achieved after 3 h of releasing the liquid nitrogen through the transfer line to the SEM chamber and a temperature of ~40 K after about 2.5 h was achieved using liquid helium. The nanomechanical experiments were done 2 h after the target temperature was reached.

We used a 5 μm -diameter tungsten carbide flat punch indenter tip coated with 5 nm of Au for the uniaxial compression experiments. The Au coating is to prevent charging of the tip for better SEM imaging. Samples were compressed at a target strain rate of 10^{-3} s^{-1} up to a total strain of 15%. Force and displacement were measured, and engineering stress and strain were calculated by dividing each by the initial cross-sectional area and pillar height, respectively. At least 4 samples were compressed for each set of phase, diameter, and temperature for assuring the accuracy of the test data.

The TEM samples of compressed nano-pillars were fabricated using the lift-out approach by utilizing a FIB, an Autoprobe™ nanomanipulator, and Pt deposition, and the region of interest was removed and fastened onto a TEM grid. The samples were then thinned using the Ga^+ source until the sample thickness of 60–65 nm was achieved. For the final thinning, a voltage of 8 KeV and a current of 42 pA were used. A FEI TEM Tecnai TFT 30 operating at 300 KeV was employed to study the lamella containing the deformed pillars. We obtained and indexed diffraction

patterns of the pillars and collected several bright-field, dark-field, and high-resolution images of the deformed microstructure.

We employed MD simulations to investigate atomic-deformation mechanisms present in a representative FCC and BCC HEA nanopillars under compression. To construct the initial sample, we created a cylindrical geometry with the axis aligned along the [324] crystallographic direction for the FCC sample and along the [001] crystallographic direction for the BCC sample to match the experiments. The initial samples were monatomic, and the HEAs were created by randomly-replacing atomic species to achieve an equi-atomic composition. The dimensions of the cylinders were 30 nm in diameter and 90 nm in length. A periodic boundary condition was prescribed in the direction parallel to the cylinder axis; and free surface-boundary conditions were prescribed in the two directions perpendicular to the axis. The energy of the initial structures was minimized, following a conjugate gradient scheme. The system was assigned a velocity profile corresponding to the simulation temperature of 50 K, 143 K, or 300 K. The pillars were then equilibrated for 200 ps at the assigned temperature and zero pressure, followed by the equilibration for 200 ps under the time integration of the microcanonical ensemble (NVE). All simulations were performed using an integration time step of 1 fs. Compression was performed by deforming the simulation box at a strain rate of 10^8 s^{-1} up to at least a total strain of 15%. Such a strain rate is an unavoidable consequence of the time scales accessible during MD simulations and may over-predict the initial yield strength in such samples. We thus restrict our discussion of the simulations to the qualitative comparison.

We implemented the embedded atom method (EAM) potential developed by Zhou, et al. [25] and chose the equi-atomic CoFeNiPd system as a representative FCC HEA and the equi-atomic AlMoWTa system as our representative BCC HEA. These systems were chosen based on (1) similarity to the experimental composition, (2) availability of inter-atomic potentials, and (3) energetic and mechanical lattice stability. The choice of a similar system for the BCC phase is further complicated by the presence of a modulated plate microstructure composed of the ordered B2 and disordered A2 lattices [13]. Despite such a complicated microstructure, it has been reported that deformation is concentrated in the disordered A2 phases [26]. Following this observation, we choose to utilize a disordered A2 lattice in our simulations. All simulations were performed using the Large-scale Atomic/Molecular Massively Parallel Simulator (LAMMPS) molecular dynamics software [27], and Open Visualization Tool (OVITO) software [28] was employed for the common neighbour analysis, calculation of atomic shear strain, and visualization.

3. Results

3.1. FCC experimental results

Fig. 1(a–c) show the stress vs. strain data for representative [324]-oriented FCC nanopillars with diameters ranging from 394 nm to 2114 nm, deformed at 295 K [Fig. 1(a)], 143 K [Fig. 1(b)], and 40 K [Fig. 1(c)]. These experiments revealed that the yield and flow stresses of samples with equivalent diameters were the highest at 40 K and lowest at 295 K. For example, the ~700 nm-diameter pillars had a yield strength of ~0.7 GPa at 295 K, 1.4 GPa at 143 K, and 1.6 GPa at 40 K. The relative increase in the yield stress with temperature appears to be lower for smaller diameter samples: the yield strength of 2 μm -diameter pillars increased by a factor of ~2.0 when temperature was lowered from 295 K to 143 K and by a factor of ~1.2 from 143 K to 40 K. For the 400-nm-diameter samples, this relative strengthening was ~1.45 and 1.25 for the same-temperature variations. The stress-strain data of the FCC pillars contains numerous stochastic bursts, whose frequency appears to increase at smaller pillar sizes and whose magnitude increases at lower temperatures for the same pillar size.

Fig. 1(a–c) also show SEM images of the typical deformation morphology of [324]-oriented FCC samples at each temperature, which

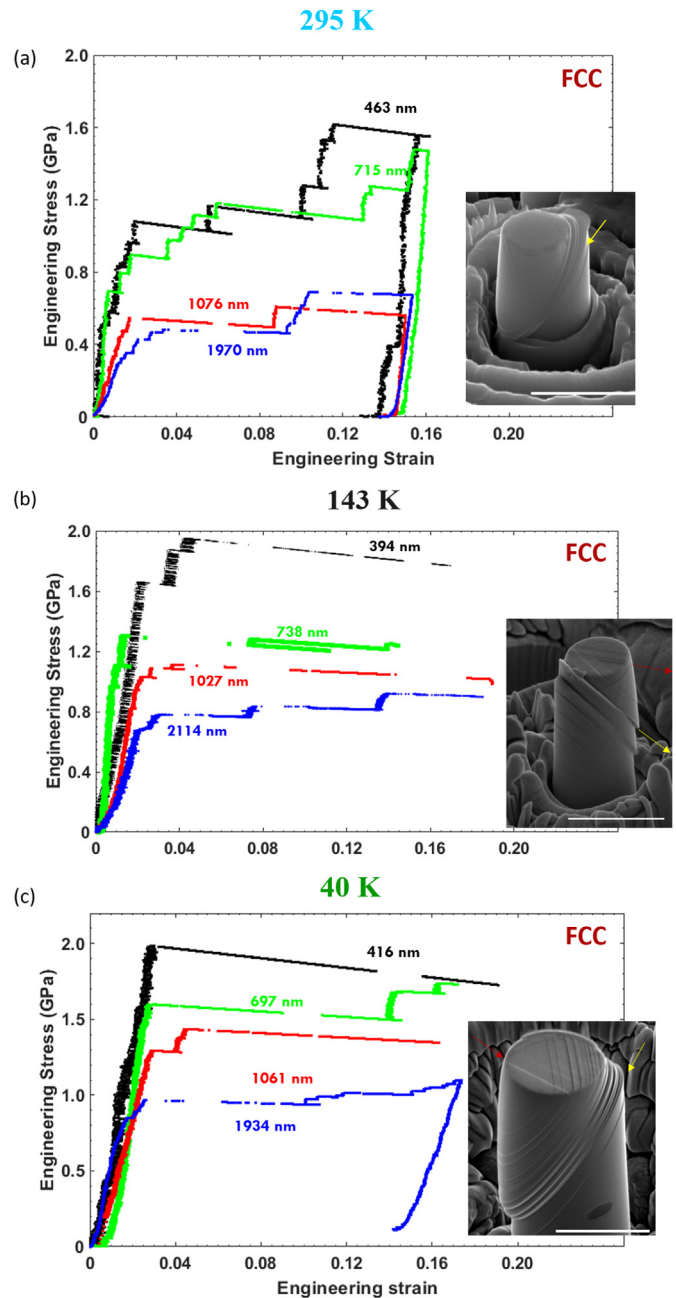


Fig. 1. Representative stress-strain curves of [324]-oriented nanopillars constructed from the FCC phase of a $\text{Al}_{0.7}\text{CoCrFeNi}$ HEA compressed at (a) 295 K, (b) 143 K, and (c) 40 K. Typical deformed 2- μm -sized nanopillars are shown as insets in the stress-strain plots at the test temperatures. The scale bar represents 3 μm . Yellow arrows (a, b, c) indicates the primary slip direction while red arrows (b, c) indicates the secondary slip direction. (For interpretation of the references to colour in this figure legend, the reader is referred to the web version of this article.)

contain multiple slip lines denoted by yellow arrows, predominantly parallel to each other and oriented at $\sim 38^\circ$ to 48° with respect to the loading direction, consistent with $\{011\}/\{111\}$ slip systems. The primary slip direction is indicated by the yellow arrows in the post-compressed pillars. The red arrows in Fig. 1(b, c) correspond to the emergence of secondary slip at the lower temperatures of 143 K and 40 K. These images and the compressive stress-strain responses suggest that the deformation mechanism remained the same at all these temperatures.

From the stress vs. strain data of the deformed FCC HEA nanopillars in Fig. 1(a–c), we observed intermittent strain bursts at room temperature and increase in flow stresses after each burst event. At low temperatures, longer strain burst regimes were observed, and we found

minimal or no increase at all in the flow stress until a strain of ~15% was reached. For example, the stress-strain curves at 295 K in Fig. 1 (a) showed that the first major strain burst event for a 400-nm-sized pillar occurred at a strain of 2%, then followed by another event at 5, 9, 10, and 12% strains till the unloading event. At 143 K in Fig. 1(b), strain hardening occurred till a 5% strain and no other strain burst activity occurred. At 40 K, apart from the burst events at yield, no other strain burst events occurred. This trend suggests that though multiple parallel slip lines were observed in the deformed pillars at the lower temperatures, these multiple slip events took place within a burst regime.

3.2. BCC experimental results

Fig. 2(a–c) present the compressive stress-strain response of nanopillars with diameters between ~400 nm and 1.8 μm, fabricated from the [001]-oriented BCC phase deformed at temperatures of 295 K [Fig. 2(a)], 143 K [Fig. 2(b)], and 40 K [Fig. 2(c)]. We observed a marginal increase in the yield strength at different temperatures for the same pillar sizes: the yield strength of a 400-nm-diameter pillar increased by 20%, from 2.5 GPa to 3.0 GPa as the temperature was lowered from 295 K to 143 K, and then by an additional 6.67%, from 3.0 GPa to 3.2 GPa as it was further lowered to 40 K. At room temperature, 2-μm-sized BCC HEA pillars had yield strengths of ~1.5 GPa, and an increase of 46% was observed in 400-nm-sized BCC HEA pillars having yield strengths of ~2.2 GPa. The deformation signature of these samples was apparently different from that of FCC pillars: the stress-strain data was smoother and less stochastic, especially for samples with diameters larger than ~2 μm.

We calculated the work hardening exponent, n , as

$$n = \frac{\partial \ln(\sigma_{12} - \sigma_6)}{\partial \ln(\varepsilon_{12} - \varepsilon_6)} \quad (1)$$

for BCC nanopillars in the strain range of 6 to 12% for all the temperatures. σ_x and ε_x indicate the measured stress and strain at the strain of $x\%$. We observed that the work-hardening exponent decreased with decreasing temperature [Fig. 2(a–c)]. For example, the work-hardening exponent calculated from the stress-strain data of 2-μm-size BCC pillars decreased from $n = 0.27$ at 295 K to 0.19 at 143 K and to 0.16 at 40 K. Fig. 2(a) shows a continuous plastic behaviour in a 2-μm-sized BCC pillar deformed at room temperature, which is different from the stochastic-plastic behaviour of smaller pillar sizes of 400 nm to 1 μm. This disparity suggests a transition from the bulk-like deformation in 2-μm-pillars to nanoscale deformation in the smaller pillars.

3.3. Size effect

Fig. 3(a) shows the plot of the yield stress of [324]-oriented FCC pillars vs. the pillar diameter deformed at each temperature. The yield strength, which is defined as the stress at the first displacement burst following the elastic regime, was determined from the stress-strain data for each pillar, examples of which are shown in Fig. 1(a–c). Error bars represent the range of stresses for each pillar dimension. This plot clearly demonstrates that the strength of pillars of all sizes consistently increased with a reduction in temperature. The highest strength in excess of 2 GPa was attained by samples with the smallest diameters of ~400 nm at 40 K, while ~2-μm-diameter pillars deformed at room temperature had the lowest strength of ~400 MPa. Fig. 3(b) shows a log-log plot of these yield stresses resolved onto {110}/⟨111⟩ slip systems and normalized by the shear modulus, G , vs. pillar diameter, D , normalized by the Burgers vector, b , at each temperature. We used the Burgers vector, $|b|$, of 0.2526 nm, calculated based on $|b| = a/2 < 110 \rangle$, where a was taken from previous XRD studies with a value of 0.3572 nm [13]. Considering the FCC phase displays a greater composition of Co, Cr, and Fe [24], G was taken as 75 GPa, common for FeCr alloys [29]. This plot reveals a power-law dependence of $\tau/G = A(D/b)^{-m}$, where m is the

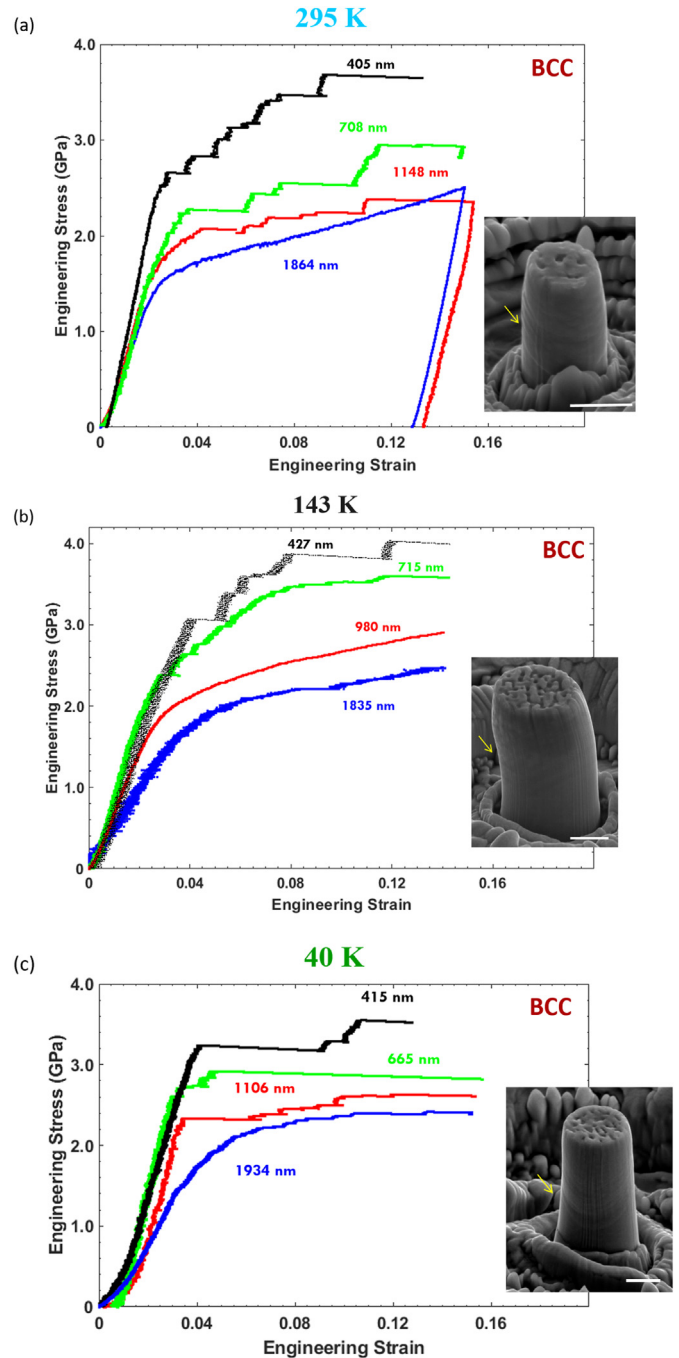


Fig. 2. Representative stress-strain curves of [001]-oriented nanopillars constructed from the BCC phase of a $\text{Al}_{0.7}\text{CoCrFeNi}$ HEA compressed at (a) 295 K, (b) 143 K, and (c) 40 K. Typical deformed 2-μm-sized nanopillars are shown in the insets of the stress-strain plots at the test temperatures. The scale bar represents 1 μm. Yellow arrows indicate the slip traces. (For interpretation of the references to colour in this figure legend, the reader is referred to the web version of this article.)

size-effect exponent that demarks each isothermal size-effect plot. It is evident that in the FCC samples, the size effect exponent decreased with temperature: from 0.68 for 295 K to 0.47 for 143 K, and to 0.38 for 40 K. We provide a summary of size-effect exponents in Table 1.

Analogously, Fig. 3(c) shows the plot of the yield stresses of ⟨001⟩-oriented BCC pillars vs. pillar diameter deformed at each temperature. These yield strengths were defined as the stresses at a 0.2% offset strain in the stress-strain data for each pillar [Fig. 2(a–c)]. The BCC data points represent the average values, and the error bars denote the standard deviation for each pillar dimension. This plot clearly demonstrates that the

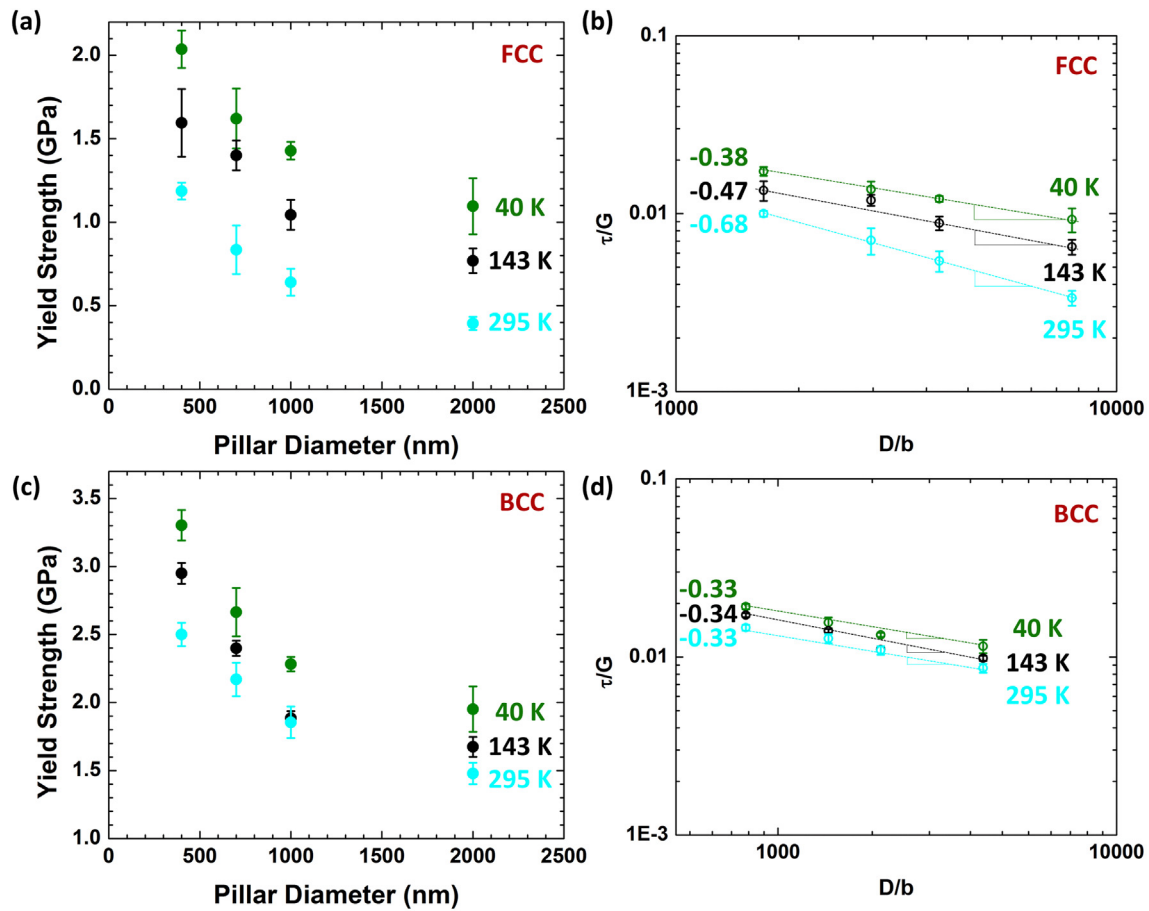


Fig. 3. (a) Un-normalized size-dependent plot of yield strength vs. pillar diameter of pillars constructed from the FCC phase of a Al_{0.7}CoCrFeNi HEA (b) Normalized size-dependent plot of the resolved shear stress vs. pillar diameter of pillars constructed from the FCC phase of a Al_{0.7}CoCrFeNi HEA (c) Un-normalized size-dependent plot of yield strength vs. pillar diameter of pillars constructed from the BCC phase of a Al_{0.7}CoCrFeNi HEA (d) Normalized size-dependent plot of the resolved shear stress vs. pillar diameter of pillars constructed from the FCC phase of a Al_{0.7}CoCrFeNi HEA.

strengths of the BCC pillars of all the sizes increased with temperature reduction. The highest strengths in excess of 3.2 GPa were attained by samples with the smallest diameters of ~400 nm at 40 K, while the largest samples, with ~2- μ m-diameters deformed at room temperature had the lowest strength of ~1.5 GPa. Fig. 3(d) shows a log-log plot of these yield stresses resolved onto the {110}/<111> slip system and normalized by the shear modulus, G , vs. pillar diameter, D , normalized by the Burgers vector, b , at each temperature. We used the Burgers vector, $|b|$, of 0.2484 nm, calculated based on $|b| = \sqrt{3}a/2\langle 111 \rangle$, where a was taken from previous XRD studies with a value of 0.2868 nm [13]. Considering the BCC phase displays a greater composition of Al and Ni [24], G was taken as 70 GPa, common for NiAl alloys [30]. This plot also reveals a power-law dependence of $\tau/G = A(D/b)^{-m}$. It is evident that in contrast to the FCC samples, the size-effect exponent remains the same at $m = 0.33$ for the BCC phase at all the temperatures.

3.4. Molecular dynamics results

To better understand the atomistic mechanisms underlying the strength and temperature dependence observed experimentally, we

Table 1
Summary of the size-effect exponents for FCC and BCC phases as also indicated in Fig. 3.

Size-effect exponent, m	40 K	143 K	295 K
FCC	0.38	0.47	0.68
BCC	0.33	0.34	0.33

performed molecular dynamics simulations on the compression of our representative Co₂₅Fe₂₅Ni₂₅Pd₂₅ FCC and Al₂₅Mo₂₅W₂₅Ta₂₅ BCC HEA systems described in the Materials and Method section (Section 2).

3.4.1. Simulated compression of the Co₂₅Fe₂₅Ni₂₅Pd₂₅ FCC HEA

Fig. 4(a–c) present the local atomic shear strain for the 30 nm-diameter FCC HEA samples compressed at 300 K, 143 K, and 50 K. These shear-strain snapshots show the accumulated shear strain up to an axial strain of 3.5% [for details of computed stress-strain data, we refer the reader to Fig. S5(a)]. Plastic deformation begins in these simulations via nucleation of a 1/6<112> partial dislocation on the surface of the initially-pristine nanopillar. A trailing partial nucleates at the same location with further straining, which creates a fully-dissociated pair of partial dislocations, which then glide along the (111) slip plane across the diameter and annihilate at the opposite surface. Further plastic deformation proceeds via the partial dislocation nucleation from the surface on planes adjacent to the previously-sheared slip planes. Partial dislocations were the primary mechanism of deformation at all the temperatures, and slip occurred on a set of parallel slip planes that correspond to those with the greatest resolved shear stress. Based on the average stress at high strains and highly-localized shear profiles in Fig. 4(a–c), it is clear that the surface steps arising from previously-nucleated dislocations (partials and their pairs) are favourable sources for subsequent dislocation nucleations, and that no cross-slip of dislocations occurred at these temperatures, which is likely related to the fact that the dislocation remains dissociated throughout the glide until annihilation at the opposing surface.

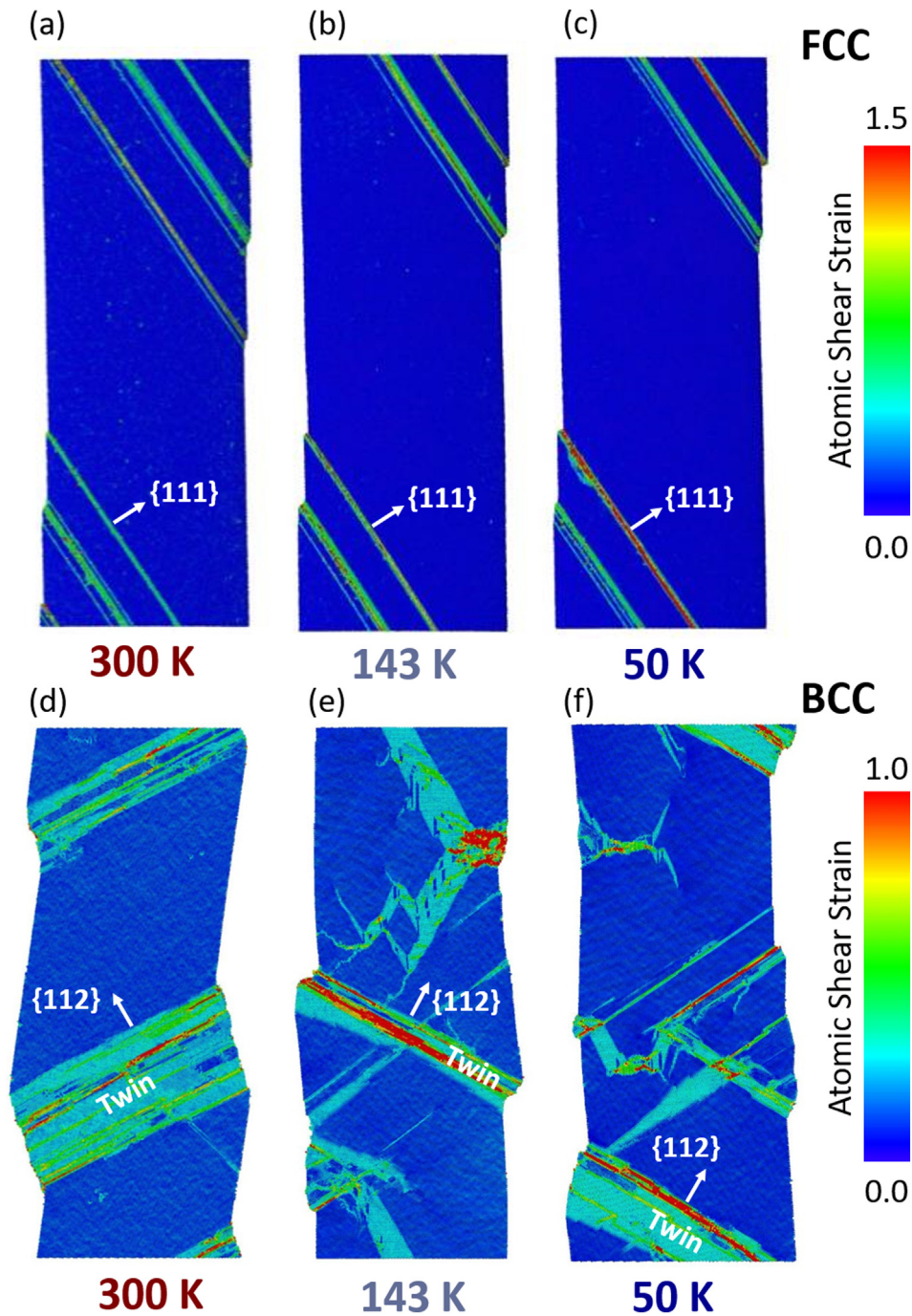


Fig. 4. Atomic shear strain of the $\langle 324 \rangle$ -oriented 30-nm-diameter $\text{Co}_{25}\text{Fe}_{25}\text{Ni}_{25}\text{Pd}_{25}$ FCC HEA deformed at (a) 50 K, (b) 143 K, and (c) 300 K to an axial strain of $\sim 3.5\%$. Deformation is dominated by the nucleation and propagation of $1/6\langle 112 \rangle$ partial dislocations on parallel slip planes that traverse the entire pillar diameter. Atomic shear strain of $\langle 001 \rangle$ -oriented 30-nm-diameter $\text{Al}_{25}\text{Mo}_{25}\text{W}_{25}\text{Ta}_{25}$ BCC HEA deformed at (d) 50 K, (e) 143 K, and (f) 300 K to the axial strain of $\sim 9\%$. Deformation is dominated by the nucleation of $1/3\langle 111 \rangle$ and $1/6\langle 111 \rangle$ partial dislocations that grow into twinned regions and nucleate full dislocations. At 50 K and 143 K, multiple slip systems are activated; slip at 300 K is confined to a set of parallel slip planes.

3.4.2. Simulated compression of the $\text{Al}_{25}\text{Mo}_{25}\text{W}_{25}\text{Ta}_{25}$ BCC HEA

Fig. 4(d–f) present the atomic shear strain of the BCC HEA sample compressed at 300 K, 143 K, and 50 K. These shear-strain snapshots show the plastic deformation patterns at an axial strain of $\sim 9\%$ [for details of the computed stress-strain data, we refer the reader to Fig. S5(b)]. Sheared regions correspond to sequences of $\langle 112 \rangle$ planes where partial dislocations have nucleated from the pillar surface and traversed the interior of the nanopillar. The nucleation of partial dislocations from the surface corresponds to the beginning of plasticity in these nanopillars. Dislocations

nucleate in groups of adjacent $\langle 112 \rangle$ planes and have Burgers vectors of $1/3\langle 111 \rangle$, $-1/6\langle 111 \rangle$, and $1/3\langle 111 \rangle$, which result in a 2-atomic-plane-thick twinned region, similar to the structure of an I_3 fault [31]. This mechanism has been discussed in greater detail in our previous work [32]. Further plastic deformation results in the nucleation of dislocations from deformed regions and thickening of twins via the nucleation and glide of $1/3\langle 111 \rangle$ partial dislocations along the boundaries of the twinned region. Due to the high symmetry of the $\langle 001 \rangle$ loading in the simulated BCC HEA, several slip systems are activated simultaneously. The bands of sheared

regions in the BCC HEA can be as low as 3-nm thick at 50 K and up to 13.6 nm thick at 300 K, i.e., 3.33–15 times thicker than sheared regions seen in the FCC HEA.

4. Discussion

The experimental results described above show three notable features in the mechanical response of FCC and BCC phases of the $\text{Al}_{0.7}\text{CoCrFeNi}$ HEA as a function of temperature. With decreasing temperature, there is (1) a significant increase in the yield strengths of both FCC and BCC samples, (2) a decrease in the work-hardening exponent in the BCC samples, and (3) a decrease in the size-effect exponent in the FCC samples.

The possible microstructural origin for these three experimental observations will be the focus of the current discussion. The initial TEM analysis indicates the dislocation slip-dominated plasticity (refer to the supplemental information, S1, Figs. S1–2). We calculated the dislocation density from the observed dislocation lines in the Dark Field (DF) image of the deformed FCC nanopillar at 40 K as $\rho_d = 2.28 \times 10^{14} \text{ m}^{-2}$ (see details in the supplementary information, S2, Fig. S3), which is greater than pure FCC metals and conventional alloys by two orders of magnitude. Such a high dislocation density has also been observed for HEAs even at room temperature [33]. We also calculated the dislocation density of the deformed BCC nanopillar at 40 K as $\rho_d = 1.40 \times 10^{14} \text{ m}^{-2}$ (see details in the supplementary information, S3, Fig. S4), which is similar to the calculated ρ_d in the FCC HEA pillars. The extent of the dislocation density, the ex-situ nature of the analysis, and artefacts from the TEM lift-out procedure make it difficult to uniquely identify a mechanism that attributes to the observed mechanical behaviour. The surface-dominated nature of the small-scale samples further complicates the interpretation of deformation mechanisms. We therefore cannot make any comments on the dominant deformation mechanisms from the TEM analysis alone.

The length scale of MD simulations offers an ideal situation to investigate dislocations in a surface-dominated HEA structure. Below, we consider our MD simulations, discuss how qualitative features of the simulated FCC and BCC HEAs may give rise to the observed experimental behaviour and compare our proposed mechanisms to literature reports.

4.1. Yield strength of FCC phase as a function of temperature

Our experiments show that the yield strengths of nanopillars fabricated from the FCC phase of this HEA are the highest at the lowest temperature of 40 K for all sample sizes: we observed the yield strength of 2.0 GPa in 400-nm-sized pillars, 1.6 GPa in 700-nm-sized pillars, and 1.3 GPa in 1 μm -sized pillars compressed at 40 K, compared with 1.1 GPa, 0.8 GPa, and 0.6 GPa in equivalent-sized samples compressed at 295 K. Fig. 2(a–c) show that the BCC HEA pillars also exhibit an increase in strength as the temperature is reduced. As the testing temperature is reduced from 295 K to 40 K, the strength of 2 μm -sized BCC HEA pillars increases from 1.5 GPa to 1.8 GPa.

The MD simulations of the representative FCC HEA show that deformation is dominated by the partial dislocation motion. Leading and trailing partials traverse the entire length of the pillar, annihilating at the surface, which precludes twinning via successive, adjacent stacking faults. The dissociation of full dislocations prevents cross-slip in the FCC HEA, promoting planar, localized plasticity and reducing strain hardening. Such dissociated partial pairs were also suggested in previous experiments on HEAs to prevent cross-slip and promote planar dislocation structures [34–36]. A previous study [37] showed the presence of size effect on the deformation twinning in a FCC HEA. In the present work, no evidence of deformation twinning in the FCC phase was observed in the post-deformation TEM analysis.

The assumed dominant deformation mode is the dislocation slip, and the relevant microstructural quantity related to the temperature-dependent strength is thus the Peierls barrier. The post-deformation morphologies of the FCC HEA shown in Fig. 1(a–c) are consistent with such a deformation mechanism. The experimental post-deformation

morphologies indicate that FCC HEA single crystals deform via parallel planar shear offsets, indicating the highly-localized plasticity at all the temperatures.

Pure metals have a virtually-non-existent Peierls barrier at low temperatures, and the contribution of lattice resistance to the yield stress does not change much with temperature [38]. Previous reports on pure metals have reported strengths for FCC metals that do not strongly depend on temperature [39,40]. Wu, et al. reported compressive strengths of bulk Ni of ~ 0.1 GPa for a temperature range of 77 K to 673 K [38]. This feature clearly differs from the strong temperature dependence of FCC HEAs observed here. In contrast, BCC metals have yield strengths that show a strong dependence upon temperature [41], consistent with BCC results presented here. The BCC metals have also shown the temperature-dependent tension-compression asymmetry and dominant slip systems that change with temperature [42].

Dilute, binary, FCC solid solutions have been reported to show temperature-dependent strengths related to solid-solution strengthening, an increase in the dislocation density and lattice distortion [38,43–46]. It was reported that at 77 K, FeNi and NiCo FCC binary alloys have yield strengths of 0.34 GPa and 0.15 GPa, respectively, while strengths at room temperature are 0.20 GPa and 0.12 GPa.

It seems reasonable to expect that FCC HEAs, as a multicomponent alloy, would display a similarly-increased temperature-dependent strength, as reported for binary FCC alloys. Indeed, significant increases in strength with decreasing temperature have been reported for a variety of FCC HEAs [36,38,47–53]. A few models have been proposed for the temperature-dependent strength in FCC HEAs [38,48,54,55]. For the deformation mechanism considered here, the model of the thermally-activated plastic flow relates the strength to internal lattice friction as [56]:

$$\frac{\tau^*(T)}{\tau^*(0)} = \frac{k_B T}{\Delta E} \ln\left(\frac{\dot{\epsilon}}{\dot{\epsilon}_0}\right) + 1, \quad (2)$$

where $\tau^*(0)$ is the athermal strength, ΔE is the activation energy required for a dislocation to overcome the dominant obstacle, $\dot{\epsilon}$ is the experimental strain rate, $\dot{\epsilon}_0$ is a reference strain rate related to the velocity of mobile dislocations, and k_B is Boltzmann's constant. Predicting strength as a function of temperature, according to Eq. (2), requires knowing the athermal strength, $\tau^*(0)$, and the energy barrier to overcome the internal obstacles, ΔE .

In conventional metallic solid solutions, the obstacles to dislocation motion are the solute atoms. No single element dominates in HEAs, which renders the definition of a “solute atom” ambiguous. Most modelling approaches begin with the classical Labusch model for strengthening in a binary alloy, which arises from the interactions of a gliding dislocation with several randomly-dispersed solutes in its glide plane, and extend it to HEAs [57]. The individual solutes in the Labusch model are not strong-pinning, i.e., are not sufficiently strong to pin a dislocation, but the combined interactions of many solutes act collectively to obstruct a gliding dislocation. For the application to FCC HEAs, Varvenne, et al. extended the Labusch model to include interactions of a gliding dislocation with an arbitrary number of solute atoms in and outside its glide plane and provided analytic expressions for $\tau^*(0)$ and ΔE [55]. In this model, initially-straight dislocations form fluctuations in order to reduce their potential energy in the presence of the heterogeneous lattice. This wavy dislocation configuration can be described by characteristic lengths, ζ_c , the length of a pinned segment, and ω_c , the length, which a dislocation segment will bow out in this wavy configuration. Analytic expressions for $\tau^*(0)$ and ΔE are:

$$\tau^*(0) = 0.051\alpha^{-1}\mu\left(\frac{1+\nu}{1-\nu}\right)^{\frac{4}{3}}f_1(\omega_c)\left(\frac{\delta_{\text{mis}}}{b^6}\right)^{\frac{2}{3}} \quad (3)$$

$$\Delta E = 0.274\alpha^{\frac{1}{3}}\mu b^3\left(\frac{1+\nu}{1-\nu}\right)^{\frac{2}{3}}f_2(\omega_c)\left(\frac{\delta_{\text{mis}}}{b^6}\right)^{\frac{1}{3}} \quad (4)$$

where α is a dimensionless number describing the dislocation line tension, μ is the shear modulus, ν is the Poisson's ratio, and b is the Burger's vector. $f_1(\omega_c)$ and $f_2(\omega_c)$ are core coefficient terms evaluated at the characteristic glide length, ω_c , and have been shown to be virtually independent of the dislocation-dissociation distance and taken as constant, 0.35 and 5.70, respectively [55]. δ_{mis} is an atomic mismatch parameter over all alloying elements and defined as

$$\delta_{mis} = \sum_n c_n \left(\Delta \bar{V}_n^2 + \sigma_{\Delta V_n}^2 \right) \quad (5)$$

where c_n is the concentration of each element, n . $\Delta \bar{V}_n$ is the misfit volume of the element, n , and defined as $\Delta \bar{V}_n = V_n - \bar{V}$ with $\bar{V} = \sum_n c_n V_n$. $\sigma_{\Delta V_n}$ is the standard deviation of the misfit volume. In the discussion below, we refer to this model as Model 1.

We would like to obtain values of $\tau^*(0)$ and ΔE for the FCC phase of our HEA to compare theoretically-predicted strengths against our experimental data. Model 1 requires several mechanical properties and atomic volumes as inputs into the model. For the FCC phase of the $Al_{0.7}CoCrFeNi$ HEA studied here, we take the atomic volumes of $V_{Co} = 11.12 \text{ \AA}^3$, $V_{Cr} = 12.27 \text{ \AA}^3$, $V_{Fe} = 12.09 \text{ \AA}^3$, and $V_{Ni} = 10.94 \text{ \AA}^3$ determined for a CoCrFeNi alloy [97]. From the EDS analysis of the FCC phase of our $Al_{0.7}CoCrFeNi$ HEA, we use $c_{Al} = 0.1$, $c_{Co} = 0.23$, $c_{Cr} = 0.26$, $c_{Fe} = 0.27$, and $c_{Ni} = 0.14$. In order to obtain V_{Ab} , we apply Vegard's law, which relates the average atomic volume of an alloy and a solute:

$$V_{Al_{0.7}CoCrFeNi, FCC} = c_{Al, FCC} V_{Al, FCC} + (1 - c_{Al, FCC}) V_{CoCrFeNi, FCC} \quad (6)$$

We relate the atomic volume to the lattice parameter for FCC crystals through $V_n = \frac{a^3}{4}$ and use lattice parameters of 0.356 nm and 0.3572 nm for CoCrFeNi [13] and the FCC phase of $Al_{0.7}CoCrFeNi$ [13], respectively. This calculation gives $V_{Al} = 13.71 \text{ \AA}^3$. Following [55], we use $\alpha = 0.123$ although in the same analysis, it was reported that at moderate temperatures, the predicted strength was insensitive to the line-tension parameter. Also following [55] and DFT calculations that show the standard deviation of the bond length in an FeCoNiCrCu HEA is only 1.6% of the mean bond length [58], we thus neglect $\sigma_{\Delta V_n}$ from the mismatch parameter. We apply the isotropic elastic constants of $\mu = 75 \text{ GPa}$ and $\nu = 0.28$ [38]. Inserting these values into Eqs. (3) and (4), we obtain $\tau^*(0) = 103.8 \text{ MPa}$ and $\Delta E = 1.17 \text{ eV}$. These values allow us to use Eq. (2) to predict the strength as a function of temperature. It should be noted that these values compare favourably to estimates of the FCC CrMnFeCoNi HEA with $\tau^*(0) = 83.0 \text{ MPa}$ and $\Delta E = 1.13 \text{ eV}$ [55].

The above model assumes that the temperature-dependent strength arises from thermal contributions to dislocations' ability to overcome internal obstacles. An alternative temperature-dependent strengthening model for HEAs has been proposed, where strengthening in FCC HEAs is assumed to arise from decreasing the dislocation core width with temperature [38]. Within the Peierls-Nabarro (P-N) model,

$$\tau = \frac{2\mu}{1-\nu} \exp\left(-\frac{2\pi\omega}{b}\right) \quad (7)$$

where ω is the dislocation width, and b is the Burgers vector, strength is exponentially related to the dislocation width. In this model, the temperature dependence of the dislocation core width is approximated as linear [38],

$$\omega = \omega_0(1 + \alpha T) \quad (8)$$

where α is a positive fitting constant, and $\omega_0 = b$. In the discussion below, we refer to this model as Model 2.

In order to compare our small-scale experimental data against these theories, we must obtain an estimate of the size-independent strength contribution. It has been argued that an estimate of the bulk strength can be obtained from the small-scale data by evaluating the size-effect

power law at a length scale that corresponds to the source length in bulk materials [34]. Following the previous analysis [34], we evaluate $\tau = A \times D^{-m}$ at $D = 20 \text{ \mu m}$ for each isothermal dataset. Fit parameters as obtained from the experimental data are $A_{300K} = 401.44 \text{ MPa}$; $A_{143K} = 679.29 \text{ MPa}$; $A_{40K} = 908.49 \text{ MPa}$, and $m_{300K} = 0.67$; $m_{143K} = 0.47$; and $m_{40K} = 0.375$. Estimations of bulk strengths are then $\tau_{300K} = 53.9 \text{ MPa}$, $\tau_{143K} = 166.2 \text{ MPa}$, and $\tau_{40K} = 295.4 \text{ MPa}$. This trend gives us an estimate of the bulk strength of the FCC phase of our HEA and enables us to compare against strengthening theories. We also fit these estimates to Model 2 and obtain fitting constant, $\alpha = 0.001 \text{ K}^{-1}$.

Fig. 5 shows these bulk strength estimates, the predictions from Model 1, and the curve fit to Model 2. It is seen that Model 1 predicts the room-temperature strength of the FCC HEA but significantly underestimates the strength at cryogenic temperatures. This feature may suggest that at low temperatures, Angstrom-level fluctuations in the dislocation line (which are neglected in Model 1) become increasingly important. The consideration of the fitting parameter, $\alpha = 0.001 \text{ K}^{-1}$, in Model 2 suggests a 23% decrease in the dislocation core width from room to cryogenic temperatures and is several orders of magnitude greater than the reported thermal expansion coefficient of $Al_{0.7}CoCrFeNi$ at $14 \times 10^{-6} \text{ K}^{-1}$ [59]. This trend suggests that Model 2 cannot capture the physical mechanism of temperature-dependent strength and is not applicable to this system. Following this analysis, it seems that Model 1 can capture near-room temperature strength well with no fitting necessary and is the most promising towards capturing the relevant underlying dislocation physics. Model 2 does not appear applicable to this system. Improvements to Model 1 at low temperatures may require the inclusion of finer fluctuations in the dislocation line.

4.2. Work hardening of the BCC phase as a function of temperature

The compression experiments show that the work-hardening exponent decreases in the BCC samples, as the temperature is decreased. Considering the high symmetry of the compression axis of BCC samples, there should be a greater activation of dislocations and dislocation sources and thus, the interaction between dislocations. From the presence of a modulated A2 and B2 microstructure [13,26], some hardening from the hard B2 phase and dislocation interactions at phase boundaries is also expected to contribute to the strength of the BCC samples. The temperature-dependent hardening exponent suggests that in addition to these strengthening mechanisms that are present in all samples, there are dislocation multiplication and storage mechanisms present,

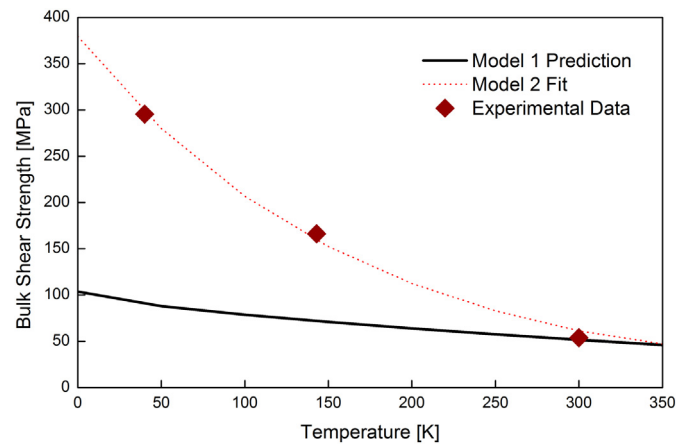


Fig. 5. Estimated bulk shear strength of the FCC phase of the $Al_{0.7}CoCrFeNi$ HEA, compared to two models of the temperature-dependent strength for FCC HEAs. Model 1 predicts the strength at room temperature well and significantly under-predicts low-temperature strengths. The Model 2 fit predicts a 23% decrease in the dislocation core width from room temperature to 0 K.

which are temperature-dependent. The post-deformation morphology revealed by SEM provided in Fig. 2(a–c) indicates the homogeneous deformation in the BCC HEA single crystals at all the temperatures. We note that previous studies identified dislocation-twin interactions as the underlying mechanism for work hardening, and hardening was observed to increase with decreasing temperature [18]. Considering that we have observed a decrease in hardening with decreasing temperature, such a mechanism may not be applicable to this BCC HEA. In contrast to previous indentation experiments [26], our TEM analysis does not indicate any phase-transformation plasticity in this BCC phase.

The MD simulations on the representative BCC HEA show highly-anisotropic dislocations. Partial dislocations are nucleated from the surface and travel through the pillar along their mixed screw/edge segment until encountering the opposing surface or an intersecting dislocation. The dislocation segment in the propagation direction is chiefly of mixed character, with the perpendicular segments showing a screw character. The shape of the dislocation after propagation indicates anisotropy in the mobility of the mixed and screw segments resulting in long, straight extended screw segments. Deformation in this simulated BCC HEA is clearly dominated by the kink-pair nucleation of screw dislocation segments. There is no evidence of the promotion of the kink-pair nucleation of screw segments in regions near solute atoms, as observed in some BCC alloys (as in the case of solid-solution softening) [60,61], which would reduce the anisotropic shape of the dislocations. The anisotropy of the dislocations also suggests that the critical resolved shear stress (CRSS) of the mixed dislocation segments is not comparable to that of the screw segments, as has been suggested in MD simulations of the dislocation motion in BCC HEAs [62].

Dislocation-multiplication mechanisms in BCC metals include double cross-slip or sources found at strong pinning points (superjogs or junctions) [63–65]. All of these mechanisms rely upon cross-slip of screw segments to multiply the dislocation content, a feature that has been noted in discussing the importance of cross-slip on the hardening behaviour in BCC metals [63–66]. As cross-slip of screw segments is a thermally-activated process, it is reasonable to expect these multiplication mechanisms to be more active at elevated temperatures and thus promote hardening at elevated temperatures.

Earlier studies on some refractory BCC HEAs have reported high strain-hardening rates at room temperature [67,68] but they did not report the effect of temperature on the work-hardening rate or propose a mechanism underlying the observed work hardening. A $\text{Ti}_{35}\text{Zr}_{27.5}\text{Hf}_{27.5}\text{Nb}_5\text{Ta}_5$ BCC HEA was reported to have high room-temperature work-hardening rates that were attributed to the transformation-induced plasticity, as indicated from the post-deformation microstructural characterization [69]. No phase transformation is expected or has been reported in this $\text{Al}_{0.7}\text{CoCrFeNi}$ HEA. Room-temperature strain hardening reported in a TiZrHfNbTa BCC HEA was attributed to the build-up of the dislocation density [70,71].

4.3. Size effect as a function of temperature

In the last decade, studies on deformation of micron- and sub-micron sized single-crystalline metals reveal a size-effect exponent of the shear stress (τ) with the pillar diameter (D), i.e., $\tau \propto D^{-m}$. In single-crystalline FCC metals, the power-law size effect has a universal exponent of $m = 0.66$ from simulations and experiments [72–76] at room temperature, which correlates well with the room-temperature size effect of $m = 0.68$ calculated for the FCC HEA nanopillars in this study. The universality of the size effect at room temperature is explained from the ease of dislocation motion and dislocation annihilation to the free surface in FCC metals [76]. It has also been shown that the sample size-effect is independent of orientations in both FCC metals [77] and BCC metals [78].

The role of thermally-activated processes in the size effect of a FCC metal was investigated by Wheeler, et al. who reported a constant size effect of $m = 0.65$ in the deformed, annealed Cu nanopillars from room temperatures to 400 °C [79]. They attributed the constant size effect to the limitation of the dislocation-source size and negligible thermally-

activated contributions to stresses within the temperature range [79]. In contrast to the previous report of the temperature insensitivity at high temperatures, we observed a reduction in the size-effect exponent, m , from 0.68 at 295 K, to 0.47 at 143 K, to 0.38 at 40 K, as well as a systematic increase in the yield strength with lowering the temperature.

Single-crystalline BCC metals also exhibit a power-law dependence of the shear stress, τ , on size. In this study, BCC HEA pillars show a similar size-effect exponent of $m = 0.33$ at test temperatures of 40 K, 143 K, and 295 K. At room temperature, single crystals of commonly-studied BCC metals (W, Ta, V, Nb, and Mo) exhibit the variation in the size-effect exponent, m , which is due to differences in their Peierls stresses and critical temperatures [76,80]. It was reported that V and Nb have low stress barriers and low critical temperatures, which enhance the screw-dislocation mobility, thus having a high size-effect exponent, m values of 0.82 at room temperature [24,80,81]. Mo, W, and Ta have the high Peierls stress and high critical temperature, leading to a reduced size-effect exponent, m (~0.32 to 0.42). The reduced screw-dislocation mobility was reported in these BCC metals ensuing the continuous plastic deformation [76,78,80–83]. Previous work on the same BCC HEA pillars demonstrated a size-effect exponent of $m = 0.28$ at room temperature [24]. Zou, et al. reported that single crystals of the refractory HEA $\text{Nb}_{25}\text{Mo}_{25}\text{Ta}_{25}\text{W}_{25}$ exhibited a size-effect exponent of $m = 0.32$ [24]. The reduced value of m at room temperature in the BCC HEAs can be attributed to their higher lattice friction than that of the pure BCC metals. We can also suggest a highly-distorted BCC phase in which the energy dispersive spectroscopy (EDS) analysis reveals ~56.9 at.% of Ni and Al [24], indicating a heavily-strained phase due to the differences in the atomic sizes of the major elements in this phase.

Experiments on the BCC HEA pillars at low temperatures of 143 K and 40 K demonstrated a size-effect exponent, m , of 0.34 and 0.33, respectively, which is similar to that at room temperature. These results are contrary to the size-effect exponents found for pure BCC metals at low temperatures. Lee, et al. [23] reported a significant decrease in m for Nb and W at 160 K, for example, m for Nb reduced from 0.73 at room temperature to 0.23 at 160 K, and m for W reduced from 0.36 at room temperature to 0.19 at 160 K. They attributed this change to the increased intrinsic lattice resistance as a result of the suppressed dislocation multiplication as the temperature reduces. From the results on compression of the BCC HEA pillars, we can suggest that at low temperatures, there is a minimal effect of temperature on the lattice resistance of BCC HEAs, in contrast to pure BCC metals, where overcoming the intrinsic lattice resistance stems almost exclusively from the thermal activation. In BCC HEAs, the lattice resistance is so high (presumably from the chemical and energetic directionality of bonds) that even with the thermal contribution during deformation at room temperature, it is similar to the deformation resistance at cryogenic temperatures. It can also be suggested that the dislocation structure in the BCC phase remains relatively stable for the range of temperatures studied, making the size-effect exponent invariant of temperature. The size-effect exponent can be governed by other phenomena, such as single arm sources [84,85]. This feature is plausible if the dislocation densities and activated slip systems during deformation remain the same [84]. Clearly, more work is needed to establish this phenomenon in the BCC HEAs.

In light of the previous discussion on temperature-dependent solution strengthening in the FCC phase of this HEA, the source of the temperature-dependent size effect becomes clear. We consider three significant contributions to the observed strength of the single-phase FCC HEA: (1) solid-solution strengthening, (2) dislocation-source contribution, which is sample size-dependent, and (3) dislocation forest interactions similar to forest hardening. These contributions to the shear strength can be represented as [84–86]:

$$\tau = \tau^* + \tau_G + \tau_{\text{source}} \propto D^{-m} \quad (9)$$

where τ^* denotes the lattice friction, τ_G is the contribution from Taylor hardening, and $\tau_{\text{source}} \propto D^{-n}$ is the contribution from the single-arm

sources, and n is the universal size-effect exponent for FCC metals. The contributions of the latter two (τ_G and τ_{source}) are temperature-independent [86,87]. Thus, the observed higher stresses at cryogenic temperatures in HEAs studied here may be understood in terms of the temperature dependence of the lattice friction, τ^* . The apparent decrease in the size-effect exponent for the FCC phase is a direct result of the increasing contribution of τ^* , as compared to τ_{source} . The τ_{source} strength contribution becomes drowned out in the increasing τ^* background lattice friction, and thus, the non-linear, power-law size effect becomes less apparent.

Although observed in the FCC HEA samples, this behaviour is similar to temperature-dependent size effects in some BCC metals with low critical temperatures, which is known to be a result of the increasing lattice resistance with decreasing temperature [88]. As has been discussed for size effects in such BCC metals [88], an increasing internal lattice resistance (τ^* term in Eq. (9)) will always result in a fit value of m that is less than the universal size exponent, n , hence the decreasing size-effect exponent reported here. The BCC HEA phase studied in the current investigation is comparable to BCC metals with high critical temperatures. The lattice friction contribution, τ^* , to shear strength at room temperature is already non-negligible, relative to τ_{source} and hence does not result in a significant change in the apparent size-effect exponent with decreasing temperature.

5. Summary and conclusion

We fabricated free-standing cylinders with diameters between 400 nm and 2 μm within the [324]-oriented FCC and [001]-oriented BCC grains of the dual-phase $\text{Al}_{0.7}\text{CoCrFeNi}$ HEA. We conducted in-situ uniaxial compression experiments at room and cryogenic temperatures and observed different size- and temperature-dependent strengthening in each phase. The size effect in the resolved shear strength at yield in both phases had a power-law form: $\tau \propto D^{-m}$, with $m = 0.68$ at 295 K, 0.47 at 143 K, and 0.38 at 40 K for the [324]-oriented FCC pillars and $m = 0.33$ for the [001]-oriented BCC phase at all temperatures. The smallest, 400-nm-diameter FCC pillars, had a 45% increase in the yield strength when deformed at 40 K, compared with that at 295 K. The strength enhancement of similar-sized BCC pillars was only 28%.

The morphological analysis of the deformed samples indicates that the low-symmetry-oriented FCC pillars undergo the single slip on multiple parallel slip planes and dislocation-mediated plasticity at all test temperatures. High-symmetry-oriented BCC pillars experience homogeneous deformation. Molecular dynamics simulations show dislocation-dominated deformation in similar FCC and BCC HEAs at all test temperatures (295 K, 143 K, and 40 K). We considered qualitative features observed in these simulations that may give rise to the observed experimental behaviour and compare these proposed mechanisms to literature reports.

We discussed size- and temperature-dependent strengthening of individual small-sized FCC and BCC HEAs in the context of existing analytical models for temperature-dependent strengthening and postulate that in FCC HEAs, it is the increasingly more dominant contribution of atomic-level fluctuations in dislocation lines at low temperatures that leads to narrowing of the local potential well, thus requiring the application of greater stresses to overcome the energy landscape. The significant increase in strengths of the FCC samples with decreasing temperature is then seen to contribute to the decrease in the exponent of the empirical size-effect power law. The virtually-unchanging size-effect exponent observed in the deformation of the micron-sized BCC HEAs at all temperatures may imply that their critical temperature is significantly higher than that of their pure metals with constituent elements, which renders the thermal activation of dislocations to be insufficient to overcome the high lattice friction during the deformation of these alloys at room and cryogenic temperatures.

These findings provide insights into the deformation and mechanical behaviour of individual crystalline phases (FCC and BCC structures) of

HEAs and may help shed light on the relationship among the chemical composition, atomic-level microstructure, and ensuing mechanical properties of these materials at different temperatures.

CRedit authorship contribution statement

Adenike M. Giwa: Methodology, Investigation, Formal analysis, Writing - original draft. **Zachary H. Aitken:** Methodology, Investigation, Formal analysis, Writing - original draft. **Peter K. Liaw:** Conceptualization, Investigation, Methodology, Resources, Writing - review & editing. **Yong-Wei Zhang:** Conceptualization, Formal analysis, Investigation, Methodology, Supervision, Writing - review & editing. **Julia R. Greer:** Conceptualization, Formal analysis, Investigation, Methodology, Supervision, Writing - review & editing.

Declaration of competing interest

The authors declare that they have no known competing financial interests or personal relationships that could have appeared to influence the work reported in this paper.

Acknowledgement

A.M.G and J.R.G. would like to thank National Science Foundation (NSF) the Stanback Space Innovation Program and the Keck Institute of Space Studies (KISS) at Caltech for the financial support of the present research. The authors acknowledge Matt H. Sullivan at the Kavli Nanoscience Institute (KNI) at Caltech for help with the TEM sample preparation and Carol Garland for her assistance with the TEM analysis and experiments. Z.H.A, M.J.Z., and Y.W.Z. gratefully acknowledge the financial support from the Agency for Science, Technology and Research (A*STAR), Singapore (Grant No. A1898b0043) and the use of computing resources at the A*STAR Computational Resource Centre, Singapore. P.K.L. very much appreciates the support of the U.S. Army Research Office project (W911NF-13-1-0438 and W911NF-19-2-0049) with the program managers, Drs. M. P. Bakas, S. N. Mathaudhu, and D. M. Stepp. PKL thanks the support from the National Science Foundation (DMR-1611180 and 1809640) with the program directors, Drs J. Yang, G. Shiflet, and D. Farkas.

Data availability

The processed size effect data required to reproduce these findings are available from the corresponding author upon request. The raw stress-strain data required to reproduce these findings cannot be shared at this time as the data also forms part of an ongoing study.

Appendix A. Supplementary data

Supplementary data to this article can be found online at <https://doi.org/10.1016/j.matdes.2020.108611>.

References

- [1] J.W. Yeh, S.K. Chen, S.J. Lin, J.Y. Gan, T.S. Chin, T.T. Shun, C.H. Tsau, S.Y. Chang, Nanostructured high-entropy alloys with multiple principal elements: novel alloy design concepts and outcomes, *Adv. Eng. Mater.* 6 (2004) 299–303, <https://doi.org/10.1002/adem.200300567>.
- [2] B. Cantor, I.T.H. Chang, P. Knight, A.J.B. Vincent, Microstructural development in equiatomic multicomponent alloys, *Mater. Sci. Eng. A* 375–377 (2004) 213–218, <https://doi.org/10.1016/j.msea.2003.10.257>.
- [3] P.-K. Huang, J.-W. Yeh, T.-T. Shun, S.-K. Chen, Multi-principal-element alloys with improved oxidation and wear resistance for thermal spray coating, *Adv. Eng. Mater.* 6 (2004) 74–78, <https://doi.org/10.1002/adem.200300507>.
- [4] Y. Zhang, T.T. Zuo, Z. Tang, M.C. Gao, K.a. Dahmen, P.K. Liaw, Z.P. Lu, Microstructures and properties of high-entropy alloys, *Prog. Mater. Sci.* 61 (2014) 1–93, <https://doi.org/10.1016/j.pmatsci.2013.10.001>.
- [5] D.B. Miracle, O.N. Senkov, A critical review of high entropy alloys and related concepts, *Acta Mater.* 122 (2017) 448–511, <https://doi.org/10.1016/j.actamat.2016.08.081>.

- [6] K.Y. Tsai, M.H. Tsai, J.W. Yeh, Sluggish diffusion in Co-Cr-Fe-Mn-Ni high-entropy alloys, *Acta Mater.* 61 (2013) 4887–4897, <https://doi.org/10.1016/j.actamat.2013.04.058>.
- [7] S. Guo, C.T. Liu, Phase stability in high entropy alloys: formation of solid-solution phase or amorphous phase, *Prog. Nat. Sci. Mater. Int.* 21 (2011) 433–446, [https://doi.org/10.1016/S1002-0071\(12\)60080-X](https://doi.org/10.1016/S1002-0071(12)60080-X).
- [8] H.Y. Diao, R. Feng, K.A. Dahmen, P.K. Liaw, Fundamental deformation behavior in high-entropy alloys: An overview, *Curr. Opin. Solid State Mater. Sci.* 21 (2017) 252–266, <https://doi.org/10.1016/j.cossms.2017.08.003>.
- [9] W.R. Wang, W.L. Wang, J.W. Yeh, Phases, microstructure and mechanical properties of Al_xCoCrFeNi high-entropy alloys at elevated temperatures, *J. Alloys Compd.* 589 (2014) 143–152, <https://doi.org/10.1016/j.jallcom.2013.11.084>.
- [10] K.B. Zhang, Z.Y. Fu, J.Y. Zhang, W.M. Wang, H. Wang, Y.C. Wang, Q.J. Zhang, J. Shi, Microstructure and mechanical properties of CoCrFeNiTiAl_x high-entropy alloys, *Mater. Sci. Eng. A* 508 (2009) 214–219, <https://doi.org/10.1016/j.msea.2008.12.053>.
- [11] Z. Tang, M.C. Gao, H. Diao, T. Yang, J. Liu, T. Zuo, Y. Zhang, Z. Lu, Y. Cheng, Y. Zhang, K. a. Dahmen, P.K. Liaw, T. Egami, Aluminum alloying effects on lattice types, microstructures, and mechanical behavior of high-entropy alloys systems, *Jom* 65 (2013) 1848–1858, <https://doi.org/10.1007/s11837-013-0776-z>.
- [12] C. Li, M. Zhao, J.C. Li, Q. Jiang, B2 structure of high-entropy alloys with addition of Al, *J. Appl. Phys.* 104 (2008), 113504, <https://doi.org/10.1063/1.3032900>.
- [13] W.-R. Wang, W.-L. Wang, S.-C. Wang, Y.-C. Tsai, C.-H. Lai, J.-W. Yeh, Effects of Al addition on the microstructure and mechanical property of Al_xCoCrFeNi high-entropy alloys, *Intermetallics* 26 (2012) 44–51, <https://doi.org/10.1016/j.intermet.2012.03.005>.
- [14] Y. Lu, Y. Dong, S. Guo, L. Jiang, H. Kang, T. Wang, B. Wen, Z. Wang, J. Jie, Z. Cao, H. Ruan, T. Li, A promising new class of high-temperature alloys: eutectic high-entropy alloys, *Sci. Rep.* 4 (2015) 6200, <https://doi.org/10.1038/srep06200>.
- [15] Y. Lu, X. Gao, L. Jiang, Z. Chen, T. Wang, J. Jie, H. Kang, Y. Zhang, S. Guo, H. Ruan, Y. Zhao, Z. Cao, T. Li, Directly cast bulk eutectic and near-eutectic high entropy alloys with balanced strength and ductility in a wide temperature range, *Acta Mater.* 124 (2017) 143–150, <https://doi.org/10.1016/j.actamat.2016.11.016>.
- [16] P. Shi, W. Ren, T. Zheng, Z. Ren, X. Hou, J. Peng, P. Hu, Y. Gao, Y. Zhong, P.K. Liaw, Enhanced strength–ductility synergy in ultrafine-grained eutectic high-entropy alloys by inheriting microstructural lamellae, *Nat. Commun.* 10 (2019) 489, <https://doi.org/10.1038/s41467-019-08460-2>.
- [17] C.L. Tracy, S. Park, D.R. Rittman, S.J. Zinkle, H. Bei, M. Lang, R.C. Ewing, W.L. Mao, High pressure synthesis of a hexagonal close-packed phase of the high-entropy alloy CrMnFeCoNi, *Nat. Commun.* 8 (2017), 15634, <https://doi.org/10.1038/ncomms15634>.
- [18] B. Gludovatz, A. Hohenwarter, D. Catoor, E.H. Chang, E.P. George, R.O. Ritchie, A fracture-resistant high-entropy alloy for cryogenic applications, *Science* (80-.) 345 (2014) 1153–1158, <https://doi.org/10.1126/science.1254581>.
- [19] Z. Zhang, M.M. Mao, J. Wang, B. Gludovatz, Z. Zhang, S.X. Mao, E.P. George, Q. Yu, R.O. Ritchie, Nanoscale origins of the damage tolerance of the high-entropy alloy CrMnFeCoNi, *Nat. Commun.* 6 (2015), 10143, <https://doi.org/10.1038/ncomms10143>.
- [20] R. Fritz, D. Wimler, A. Leitner, V. Maier-Kiener, D. Kiener, Dominating deformation mechanisms in ultrafine-grained chromium across length scales and temperatures, *Acta Mater.* 140 (2017) 176–187, <https://doi.org/10.1016/j.actamat.2017.08.043>.
- [21] A.S. Schneider, *Mechanical Properties of Small-Scale BCC Metal Structures*, 2010.
- [22] B. Bhushan, *Nanotribology and Nanomechanics*, Springer International Publishing, Cham, 2017, <https://doi.org/10.1007/978-3-319-51433-8>.
- [23] S.-W. Lee, Y. Cheng, I. Ryu, J.R. Greer, Cold-temperature deformation of nano-sized tungsten and niobium as revealed by in-situ nano-mechanical experiments, *Sci. China Technol. Sci.* 57 (2014) 652–662, <https://doi.org/10.1007/s11431-014-5502-8>.
- [24] A.M. Giwa, P.K. Liaw, K.A. Dahmen, J.R. Greer, Microstructure and small-scale size effects in plasticity of individual phases of Al_{0.7}CoCrFeNi high entropy alloy, *Extrem. Mech. Lett.* 8 (2016) 220–228, <https://doi.org/10.1016/j.eml.2016.04.013>.
- [25] X.W. Zhou, R.A. Johnson, H.N.G. Wadley, Misfit-energy-increasing dislocations in vapor-deposited CoFe/NiFe multilayers, *Phys. Rev. B* 69 (2004), 144113, <https://doi.org/10.1103/PhysRevB.69.144113>.
- [26] I. Basu, V. Ocelik, J.T.M. De Hosson, Size dependent plasticity and damage response in multiphase body centered cubic high entropy alloys, *Acta Mater.* 150 (2018) 104–116, <https://doi.org/10.1016/j.actamat.2018.03.015>.
- [27] S. Plimpton, Fast parallel algorithms for short-range molecular dynamics, *J. Comp. Phys.* 117 (1995) 1–19, <https://doi.org/10.1006/jcph.1995.1039>.
- [28] A. Stukowski, Visualization and analysis of atomistic simulation data with OVITO—the open visualization tool, *Model. Simul. Mater. Sci. Eng.* 18 (2009) 15012, <https://doi.org/10.1088/0965-0393/18/1/015012>.
- [29] F. Louchet, From individual dislocation motion to collective behaviour, *J. Mater. Sci.* 41 (2006) 2641–2646, <https://doi.org/10.1007/s10853-006-7827-6>.
- [30] D.B. Miracle, R. Darolia, NiAl and its alloys, *Struct. Appl. Internet. Compd.* 2 (2000) 20.
- [31] J.P. Hirth, J. Lothe, *Theory of Dislocations*, Second Ed., John Wiley & Sons, Inc, New York, 1982.
- [32] Z.H. Aitken, Y.-W. Zhang, Revealing the deformation twinning nucleation mechanism of BCC HEAs, *MRS Commun* 9 (2019) 406–412, <https://doi.org/10.1557/mrc.2019.16>.
- [33] J.Y. He, H. Wang, H.L. Huang, X.D. Xu, M.W. Chen, Y. Wu, X.J. Liu, T.G. Nieh, K. An, Z.P. Lu, A precipitation-hardened high-entropy alloy with outstanding tensile properties, *Acta Mater.* 102 (2016) 187–196.
- [34] N.L. Okamoto, S. Fujimoto, Y. Kambara, M. Kawamura, Z.M.T. Chen, H. Matsunoshita, K. Tanaka, H. Inui, E.P. George, Size effect, critical resolved shear stress, stacking fault energy, and solid solution strengthening in the CrMnFeCoNi high-entropy alloy, *Sci. Rep.* 6 (2016), 35863, <https://doi.org/10.1038/srep35863>.
- [35] I.V. Kireeva, Y.I. Chumlyakov, Z.V. Pobedennaya, A.V. Vyrodova, I.V. Kuksgauzen, V.V. Poklonov, D.A. Kuksgauzen, The orientation dependence of critical shear stresses in Al_{0.3}CoCrFeNi high-entropy alloy single crystals, *Tech. Phys. Lett.* 43 (2017) 615–618, <https://doi.org/10.1134/S1063785017070082>.
- [36] F. Otto, A. Dlouhý, C. Somsen, H. Bei, G. Eggeler, E.P. George, The influences of temperature and microstructure on the tensile properties of a CoCrFeMnNi high-entropy alloy, *Acta Mater.* 61 (2013) 5743–5755, <https://doi.org/10.1016/j.actamat.2013.06.018>.
- [37] Z.Y. Liang, J.T.M. De Hosson, M.X. Huang, Size effect on deformation twinning in face-centred cubic single crystals: experiments and modelling, *Acta Mater.* 129 (2017) 1–10, <https://doi.org/10.1016/j.actamat.2017.02.063>.
- [38] Z. Wu, H. Bei, G.M. Pharr, E.P. George, Temperature dependence of the mechanical properties of equiatomic solid solution alloys with face-centered cubic crystal structures, *Acta Mater.* 81 (2014) 428–441, <https://doi.org/10.1016/j.actamat.2014.08.026>.
- [39] M.F. Ashby, H.J. Frost, *Deformation-Mechanism Maps*, Oxford Pergamon Press, 1982 44–45.
- [40] H.M. Rosenberg, The properties of metals at low temperatures, *Prog. Met. Phys.* 7 (1958) 339–394, [https://doi.org/10.1016/0502-8205\(58\)90007-8](https://doi.org/10.1016/0502-8205(58)90007-8).
- [41] D. Brunner, V. Glebovsky, The plastic properties of high-purity W single crystals, *Mater. Lett.* 42 (2000) 290–296, [https://doi.org/10.1016/S0167-577X\(99\)00200-1](https://doi.org/10.1016/S0167-577X(99)00200-1).
- [42] J.A. Shields, S.H. Goods, R. Gibala, T.E. Mitchell, Deformation of high purity tantalum single crystals at 4.2 K, *Mater. Sci. Eng.* 20 (1975) 71–81, [https://doi.org/10.1016/0025-5416\(75\)90132-9](https://doi.org/10.1016/0025-5416(75)90132-9).
- [43] P. Feltham, G. Copley, Yielding and work-hardening in alpha-brasses, *Acta Metall.* 8 (1960) 542–550, [https://doi.org/10.1016/0001-6160\(60\)90108-5](https://doi.org/10.1016/0001-6160(60)90108-5).
- [44] H. Traub, H. Neuhäuser, C. Schwink, Investigations of the yield region of concentrated Cu-Ge and Cu-Zn single crystals—I. critical resolved shear stress, slip line formation and the true strain rate, *Acta Metall.* 25 (1977) 437–446, [https://doi.org/10.1016/0001-6160\(77\)90234-6](https://doi.org/10.1016/0001-6160(77)90234-6).
- [45] G.W. Ardley, A.H. Cottrell, Yield points in brass crystals, *Proc. R. Soc. London. Ser. A. Math. Phys. Sci.* 219 (1953) 328–340, <https://doi.org/10.1098/rspa.1953.0150>.
- [46] V. Subramanya Sarma, K. Sivaprasad, D. Sturm, M. Heilmäier, Microstructure and mechanical properties of ultra fine grained Cu–Zn and Cu–Al alloys produced by cryorolling and annealing, *Mater. Sci. Eng. A* 489 (2008) 253–258, <https://doi.org/10.1016/j.msea.2007.12.016>.
- [47] S.I. Rao, C. Woodward, T.A. Parthasarathy, O. Senkov, Atomistic simulations of dislocation behavior in a model FCC multicomponent concentrated solid solution alloy, *Acta Mater.* 134 (2017) 188–194, <https://doi.org/10.1016/j.actamat.2017.05.071>.
- [48] Z. Wu, Y. Gao, H. Bei, Thermal activation mechanisms and Labusch-type strengthening analysis for a family of high-entropy and equiatomic solid-solution alloys, *Acta Mater.* 120 (2016) 108–119, <https://doi.org/10.1016/j.actamat.2016.08.047>.
- [49] Z. Wu, Y.F. Gao, H. Bei, Single crystal plastic behavior of a single-phase, face-centered-cubic-structured, equiatomic FeNiCrCo alloy, *Scr. Mater.* 109 (2015) 108–112, <https://doi.org/10.1016/j.scriptamat.2015.07.031>.
- [50] Z. Wu, H. Bei, F. Otto, G.M. Pharr, E.P. George, Recovery, recrystallization, grain growth and phase stability of a family of FCC-structured multi-component equiatomic solid solution alloys, *Intermetallics* 46 (2014) 131–140, <https://doi.org/10.1016/j.intermet.2013.10.024>.
- [51] S.I. Hong, J. Moon, S.K. Hong, H.S. Kim, Thermally activated deformation and the rate controlling mechanism in CoCrFeMnNi high entropy alloy, *Mater. Sci. Eng. A* 682 (2017) 569–576, <https://doi.org/10.1016/j.msea.2016.11.078>.
- [52] I. Kireeva, Y. Chumlyakov, Z. Pobedennaya, A. Vyrodova, Temperature dependence of mechanical properties in [111]-oriented single crystals of CoCrFeNiAl_{0.3} high entropy alloy, *AIP Conf. Proc.* 1909 (2017) 020083, <https://doi.org/10.1063/1.5013764>.
- [53] G. Laplanche, J. Bonneville, C. Varvenne, W.A. Curtin, E.P. George, Thermal activation parameters of plastic flow reveal deformation mechanisms in the CrMnFeCoNi high-entropy alloy, *Acta Mater.* 143 (2018) 257–264, <https://doi.org/10.1016/j.actamat.2017.10.014>.
- [54] I. Toda-Caraballo, P.E.J. Rivera-Díaz-del-Castillo, Modelling solid solution hardening in high entropy alloys, *Acta Mater.* 85 (2015) 14–23, <https://doi.org/10.1016/j.actamat.2014.11.014>.
- [55] C. Varvenne, A. Luque, W.A. Curtin, Theory of strengthening in fcc high entropy alloys, *Acta Mater.* 118 (2016) 164–176, <https://doi.org/10.1016/j.actamat.2016.07.040>.
- [56] D. Hull, D.J. Bacon, *Introduction to Dislocations*, fourth ed. Butterworth-Heinemann, Oxford, 2001.
- [57] R. Labusch, A statistical theory of solid solution hardening, *Phys. Status Solidi* 41 (1970) 659–669, <https://doi.org/10.1002/pssb.19700410221>.
- [58] S. Liu, Y. Wei, The Gaussian distribution of lattice size and atomic level heterogeneity in high entropy alloys, *Extrem. Mech. Lett.* 11 (2017) 84–88, <https://doi.org/10.1016/j.eml.2016.10.007>.
- [59] H.-P. Chou, Y.-S. Chang, S.-K. Chen, J.-W. Yeh, Microstructure, thermophysical and electrical properties in Al_xCoCrFeNi (0 ≤ x ≤ 2) high-entropy alloys, *Mater. Sci. Eng. B* 163 (2009) 184–189, <https://doi.org/10.1016/j.mseb.2009.05.024>.
- [60] R.J. Arsenault, Low temperature of deformation of bcc metals and their solid-solution alloys, *Treatise Mater. Sci. Technol* 1975, pp. 1–99, <https://doi.org/10.1016/B978-0-12-341806-7.50008-8>.
- [61] A. Sato, M. Meshii, Solid solution softening and solid solution hardening, *Acta Metall.* 21 (1973) 753–768, [https://doi.org/10.1016/0001-6160\(73\)90040-0](https://doi.org/10.1016/0001-6160(73)90040-0).
- [62] S.I. Rao, C. Varvenne, C. Woodward, T.A. Parthasarathy, D. Miracle, O.N. Senkov, W.A. Curtin, Atomistic simulations of dislocations in a model BCC multicomponent concentrated solid solution alloy, *Acta Mater.* 125 (2017) 311–320, <https://doi.org/10.1016/j.actamat.2016.12.011>.
- [63] F. Louchet, L.P. Kubin, Dislocation processes in B.C.C. metals, *Phys. Status Solidi* 56 (1979) 169–176, <https://doi.org/10.1002/pssa.2210560117>.

- [64] F. Louchet, L.P. Kubin, D. Vesely, In situ deformation of b.c.c. crystals at low temperatures in a high-voltage electron microscope dislocation mechanisms and strain-rate equation, *Philos. Mag. A* 39 (1979) 433–454, <https://doi.org/10.1080/01418617908239283>.
- [65] B. Šesták, A. Seeger, The relationship between the work-hardening of B.C.C. and F.C.C. metals, *Phys. Status Solidi* 43 (1971) 433–444, <https://doi.org/10.1002/pssb.2220430146>.
- [66] T. Takeuchi, Theory of low temperature work-hardening of body-centred cubic metals, *J. Phys. Soc. Jpn.* 27 (1969) 436–443, <https://doi.org/10.1143/JPSJ.27.436>.
- [67] O.N. Senkov, J.M. Scott, S.V. Senkova, F. Meisenkothen, D.B. Miracle, C.F. Woodward, Microstructure and elevated temperature properties of a refractory TaNbHfZrTi alloy, *J. Mater. Sci.* 47 (2012) 4062–4074, <https://doi.org/10.1007/s10853-012-6260-2>.
- [68] O.N. Senkov, S.V. Senkova, D.B. Miracle, C. Woodward, Mechanical properties of low-density, refractory multi-principal element alloys of the Cr–Nb–Ti–V–Zr system, *Mater. Sci. Eng. A* 565 (2013) 51–62, <https://doi.org/10.1016/j.msea.2012.12.018>.
- [69] L. Liliensten, J.-P. Couzinié, J. Bourgon, L. Perrière, G. Dirras, F. Prima, I. Guillot, Design and tensile properties of a bcc Ti-rich high-entropy alloy with transformation-induced plasticity, *Mater. Res. Lett.* 5 (2017) 110–116, <https://doi.org/10.1080/21663831.2016.1221861>.
- [70] J.-P. Couzinié, L. Liliensten, Y. Champion, G. Dirras, L. Perrière, I. Guillot, On the room temperature deformation mechanisms of a TiZrHfNbTa refractory high-entropy alloy, *Mater. Sci. Eng. A* 645 (2015) 255–263, <https://doi.org/10.1016/j.msea.2015.08.024>.
- [71] L. Liliensten, J.-P. Couzinié, L. Perrière, A. Hocini, C. Keller, G. Dirras, I. Guillot, Study of a bcc multi-principal element alloy: tensile and simple shear properties and underlying deformation mechanisms, *Acta Mater.* 142 (2018) 131–141, <https://doi.org/10.1016/j.actamat.2017.09.062>.
- [72] C.P. Frick, B.G. Clark, S. Orso, a.S. Schneider, E. Arzt, Size effect on strength and strain hardening of small-scale [1 1 1] nickel compression pillars, *Mater. Sci. Eng. A* 489 (2008) 319–329, <https://doi.org/10.1016/j.msea.2007.12.038>.
- [73] A. Kunz, S. Pathak, J.R. Greer, Size effects in Al nanopillars: single crystalline vs. bicrystalline, *Acta Mater.* 59 (2011) 4416–4424, <https://doi.org/10.1016/j.actamat.2011.03.065>.
- [74] J.R. Greer, W.C. Oliver, W.D. Nix, Size dependence of mechanical properties of gold at the micron scale in the absence of strain gradients, *Acta Mater.* 53 (2005) 1821–1830, <https://doi.org/10.1016/j.actamat.2004.12.031>.
- [75] A.T. Jennings, M.J. Burek, J.R. Greer, Microstructure versus size: mechanical properties of electroplated single crystalline Cu Nanopillars, *Phys. Rev. Lett.* 104 (2010), 135503, <https://doi.org/10.1103/PhysRevLett.104.135503>.
- [76] J.R. Greer, J.T.M. De Hosson, Plasticity in small-sized metallic systems: intrinsic versus extrinsic size effect, *Prog. Mater. Sci.* 56 (2011) 654–724, <https://doi.org/10.1016/j.pmatsci.2011.01.005>.
- [77] R. Dou, B. Derby, A universal scaling law for the strength of metal micropillars and nanowires, *Scr. Mater.* 61 (2009) 524–527, <https://doi.org/10.1016/j.scriptamat.2009.05.012>.
- [78] A.S. Schneider, C.P. Frick, B.G. Clark, P.A. Gruber, E. Arzt, Influence of orientation on the size effect in bcc pillars with different critical temperatures, *Mater. Sci. Eng. A* 528 (2011) 1540–1547, <https://doi.org/10.1016/j.msea.2010.10.073>.
- [79] J.M. Wheeler, C. Kirchlechner, J.S. Micha, J. Michler, D. Kiener, The effect of size on the strength of FCC metals at elevated temperatures: annealed copper, *Philos. Mag.* 96 (2016) 3379–3395, <https://doi.org/10.1080/14786435.2016.1224945>.
- [80] A.S. Schneider, B.G. Clark, C.P. Frick, P.A. Gruber, E. Arzt, Effect of orientation and loading rate on compression behavior of small-scale Mo pillars, *Mater. Sci. Eng. A* 508 (2009) 241–246, <https://doi.org/10.1016/j.msea.2009.01.011>.
- [81] S. Brinckmann, J.Y. Kim, J.R. Greer, Fundamental differences in mechanical behavior between two types of crystals at the nanoscale, *Phys. Rev. Lett.* 100 (2008) 1–4, <https://doi.org/10.1103/PhysRevLett.100.155502>.
- [82] J.-Y. Kim, J.R. Greer, Size-dependent mechanical properties of molybdenum nanopillars, *Appl. Phys. Lett.* 93 (2008), 101916, <https://doi.org/10.1063/1.2979684>.
- [83] J.Y. Kim, D. Jang, J.R. Greer, Tensile and compressive behavior of tungsten, molybdenum, tantalum and niobium at the nanoscale, *Acta Mater.* 58 (2010) 2355–2363, <https://doi.org/10.1016/j.actamat.2009.12.022>.
- [84] S.-W. Lee, W.D. Nix, Size dependence of the yield strength of fcc and bcc metallic micropillars with diameters of a few micrometers, *Philos. Mag.* 92 (2012) 1238–1260, <https://doi.org/10.1080/14786435.2011.643250>.
- [85] Y. Zou, S. Maiti, W. Steurer, R. Spolenak, Size-dependent plasticity in an Nb₂₅Mo₂₅Ta₂₅W₂₅ refractory high-entropy alloy, *Acta Mater.* 65 (2014) 85–97, <https://doi.org/10.1016/j.actamat.2013.11.049>.
- [86] T.A. Parthasarathy, S.I. Rao, D.M. Dimiduk, M.D. Uchic, D.R. Trinkle, Contribution to size effect of yield strength from the stochastics of dislocation source lengths in finite samples, *Scr. Mater.* 56 (2007) 313–316, <https://doi.org/10.1016/j.scriptamat.2006.09.016>.
- [87] S.I. Rao, D.M. Dimiduk, T.A. Parthasarathy, M.D. Uchic, M. Tang, C. Woodward, Athermal mechanisms of size-dependent crystal flow gleaned from three-dimensional discrete dislocation simulations, *Acta Mater.* 56 (2008) 3245–3259, <https://doi.org/10.1016/j.actamat.2008.03.011>.
- [88] S. Min Han, G. Feng, J. Young Jung, H. Joon Jung, J.R. Groves, W.D. Nix, Y. Cui, Critical-temperature/Peierls-stress dependent size effects in body centered cubic nanopillars, *Appl. Phys. Lett.* 102 (2013), 041910, <https://doi.org/10.1063/1.4776658>.